JOURNAL OF MATERIALS SCIENCE 26 (1991) 1531–1544

Heterogeneous nucleation of solidification of cadmium particles embedded in an aluminium matrix

D. L. ZHANG*, K. CHATTOPADHYAY‡, B. CANTOR*
*Centre for Advanced Materials and Composites, Department of Materials, Oxford University, Parks Road, Oxford OX1 3PH, UK
‡Department of Metallurgy, Indian Institute of Science, Bangalore 560012, India

A hypomonotectic alloy of Al–4.5wt%Cd has been manufactured by melt spinning and the resulting microstructure examined by transmission electron microscopy. As-melt spun hypomonotectic Al–4.5wt%Cd consists of a homogeneous distribution of faceted 5 to 120 nm diameter cadmium particles embedded in a matrix of aluminium, formed during the monotectic solidification reaction. The cadmium particles exhibit an orientation relationship with the aluminium matrix of $\{111\}_{Al}//\{0001\}_{Cd}$ and $\langle 110\rangle_{Al}//\langle 11\bar{2}0\rangle_{Cd}$, with four cadmium particle variants depending upon which of the four $\{111\}_{Al}$ planes is parallel to $\{0001\}_{Cd}$. The cadmium particles exibit a distorted cuboctahedral shape, bounded by six curved $\{100\}_{Al}//\{20\bar{2}3\}_{Cd}$ facets, six curved $\{111\}_{Al}/\{40\bar{4}3\}_{Cd}$ facets and two flat $\{111\}_{Al}//\{0001\}_{Cd}$ facets. The as-melt spun cadmium particle shape is metastable and the cadmium particles equilibrate during heat treatment below the cadmium melting point, becoming elongated to increase the surface area and decrease the separation of the $\{111\}_{Al}//\{0001\}_{Cd}$ facets.

The equilibrium cadmium particle shape and, therefore, the anisotropy of solid aluminium–solid cadmium and solid aluminium –liquid cadmium surface energies have been monitored by *in situ* heating in the transmission electron microscope over the temperature range between room temperature and 420 °C. The anisotropy of solid aluminium–solid cadmium surface energy is constant between room temperature and the cadmium melting point, with the $\{100\}_{Al}//\{20\bar{2}3\}_{Cd}$ surface energy on average 40% greater than the $\{111\}_{Al}//\{0001\}_{Cd}$ surface energy, and 10% greater than the $\{111\}_{Al}//\{40\bar{4}3\}_{Cd}$ surface energy. When the cadmium particles melt at temperatures above 321 °C, the $\{100\}_{Al}//\{20\bar{2}3\}_{Cd}$ facets disappear and the $\{111\}_{Al}//\{40\bar{4}3\}_{Cd}$ and $\{111\}_{Al}//\{0001\}_{Cd}$ surface energies become equal. The $\{111\}_{Al}$ facets do not disappear when the cadmium particles melt, and the anisotropy of solid aluminium–liquid cadmium surface energy decreases gradually with increasing temperature above the cadmium melting point.

The kinetics of cadmium solidification have been examined by heating and cooling experiments in a differential scanning calorimeter over a range of heating and cooling rates. Cadmium particle solidification is nucleated catalytically by the surrounding aluminium matrix on the $\{111\}_{Al}$ faceted surfaces, with an undercooling of 56 K and a contact angle of 42°. The nucleation kinetics of cadmium particle solidification are in good agreement with the hemispherical cap model of heterogeneous nucleation.

1. Introduction

The nucleation of solidification in ingots and castings is important in determining microstructural features such as phase composition, grain size and structure, and distribution of second phase particles, all of which influence the final material properties. Nucleation of solidification usually takes place by a heterogeneous process, with solid nuclei forming on an external catalytic surface. Unfortunately there are serious experimental difficulties in studying the heterogeneous nucleation of solidification in ingots and castings [1–3], because of the difficulty of excluding extraneous impurities which could otherwise act as catalysts. The most common method of trying to reduce impurity effects has been to study small, typically 1 to 100 μm sized liquid droplets. Organic emulsifying agents have been used to prepare a liquid foam [4–15], and individual droplets have been studied on carefully prepared substrates [16–22], without substrates in flight tubes [23–27], by levitation [28], or after fluxing to scavenge unwanted impurities [29–35]. In most of these experimental studies, a technique such as calorimetry, dilatometry or microscopy has been used to monitor the onset of solidification, so as to determine

0022–2461/91 $03.00 + .12

the thermal driving force needed in the liquid to overcome the kinetic barrier to nucleation. Unfortunately, the reported measurements of liquid undercooling are far from reproducible [3].

An experimental technique which gives more reproducible measurements of liquid undercooling was first devised by Wang and Smith [36] and subsequently used by Chadwick and co-workers [37–39]. A binary alloy is thermomechanically manipulated to produce a microstructure of low melting point particles embedded in a high melting point matrix, and is then heat treated to monitor the solidification behaviour of the particles. Embedded particle experiments of this type are particularly suitable for controlled studies of heterogeneous nucleation, with the solidification of the particles nucleated catalytically by the surrounding high melting point matrix. Recently, Moore *et al.* [3] have shown that embedded particle nucleation experiments can be improved by using a monotectic binary alloy prepared by rapid solidification. A monotectic alloy system ensures that the embedded particles are insoluble in the matrix at low temperature, so that the thermodynamics of solidification are not influenced by solubility effects. Alloy preparation by rapid solidification ensures that the embedded particles are extremely small, so that extraneous impurities are segregated into an insignificant number of particles, and so that the morphology and crystallography of the particles can be examined in detail by transmission electron microscopy. Moore *et al.* [3] investigated the solidification behaviour of lead particles embedded in an aluminium matrix in rapidly solidified hypermonotectic Al–5wt%Pb. The present paper describes the results of a similar investigation into the solidification of cadmium particles embedded in an aluminium matrix in rapidly solidified hypomonotectic Al–4.5wt%Cd.

3. Experimental technique

Hypomonotectic Al–4.5wt%Cd ingots were manufactured by induction melting 99.999% pure aluminium and cadmium in recrystallized alumina crucibles under a dynamic argon atmosphere. Specimens of each alloy ingot were rapidly solidified by melt spinning [40]. Alloy charges of approximately 5 g were induction remelted in quartz crucibles under a dynamic argon atmosphere, and then ejected at a superheat of 70 K with an argon overpressure of 20 kPa through a $1 \times 5\ mm^2$ orifice onto the outer surface of a polished copper wheel rotating with a tangential surface speed of $22\ m\ sec^{-1}$. The resulting melt-spun ribbons were typically 0.2 mm in thickness, 8 mm in width and several metres in length. The ribbon compositions were examined in a Cameca Camebax electron microprobe analyser and determined to be 4.47wt%Cd. To check for possible non-equilibrium solidification effects, some specimens of the melt-spun ribbons were equilibrated by annealing under a dynamic argon atmosphere for either (a) 10^5 sec at 300 °C, just below the cadmium melting point of 321 °C, or (b) 300 sec at 350 °C, just above the cadmium melting point. As-melt spun and annealed specimens were jet-electropolished in a mixture of 25vol% nitric acid and 75vol% methanol at − 40 °C for metallographic examination in JEOL 100C and Philips CM12 transmission electron microscopes.

The solidification behaviour of cadmium particles in the as-melt spun and annealed Al–4.5wt%Cd alloys were investigated in a Dupont 1090 thermal analyser fitted with 910 differential scanning calorimeter module. Individual 15 to 20 mg samples were sealed in aluminium cans, heated from 230 to 350 °C at a heating rate of $10\ K\ min^{-1}$, held for 300 sec, and then re-cooled to 230 °C at a cooling rate in the range 0.5 to $10\ K\ min^{-1}$, all under a dynamic argon atmosphere. During each heating and cooling cycle, the differences in heat flow to and from the sample and a similarly heat treated reference were continuously recorded at maximum sensitivity on a microcomputer for subsequent examination.

3. Results

3.1. Alloy microstructures

Fig. 1 shows a typical transmission electron micrograph of the microstructure of as-melt spun hypomonotectic Al–4.5wt%Cd, consisting of small cadmium particles homogeneously distributed throughout a matrix of aluminium. Fig. 2a and b show the as-melt spun cadmium particle size distribution by number and volume respectively. The cadmium particles ranged from 5 to 120 nm in diameter, with an average particle diameter of 20 nm, and an average interparticle spacing of 140 nm. The cadmium particles were resistant to heat treatment, with insignificant coarsening after 300 sec at 350 °C or 10^5 sec at 300 °C.

The cadmium particles were faceted in as-melt spun Al–4.5wt%Cd. To establish the facet crystallography, superimposed aluminium and cadmium electron diffraction patterns were generated to determine the aluminium–cadmium orientation relationship, and then the cadmium particle cross-sectional shape was examined as a function of aluminium matrix crystallographic orientation. This was achieved by tilting until a low index aluminium zone axis was parallel to

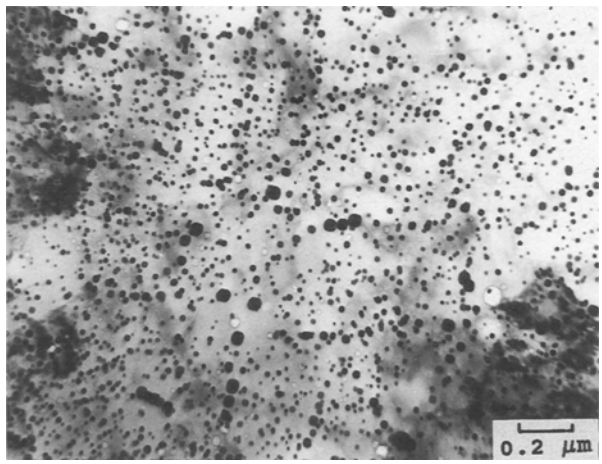

Figure 1 Bright field transmission electron micrograph of as-melt spun hypomonotectic Al–4.5wt%Cd, showing a homogeneous distribution of Cd particles embedded in an aluminium matrix.

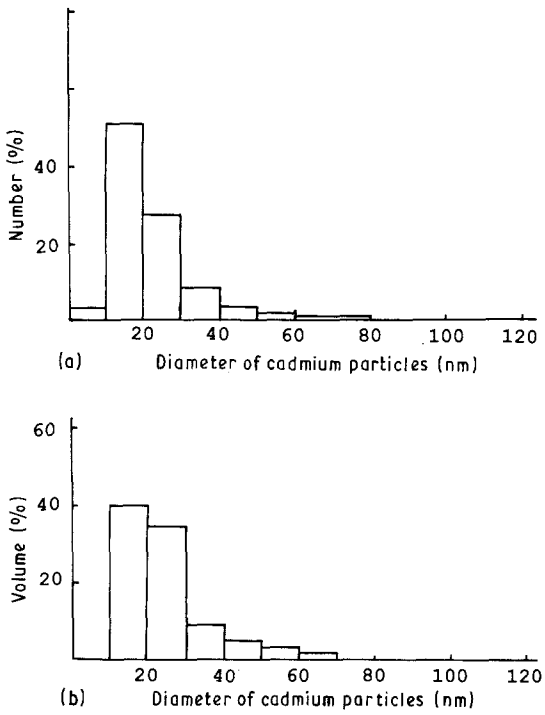

Figure 2 Size distribution of cadmium particles in as-melt spun Al–4.5wt%Cd by (a) number and (b) volume.

electron beam, as shown by a symmetrical distribution of Kikuchi lines and/or diffraction spots, followed by recording the diffraction pattern together with the corresponding bright field and dark field images.

The h c p cadmium particles were found to have an orientation relationship with the f c c aluminium matrix which can be described as

$$\{111\}_{Al}//\{0001\}_{Cd}$$

$$\langle 110\rangle_{Al}//\langle 11\bar{2}0\rangle_{Cd}$$

Each cadmium particle was a single crystal, and in each aluminium grain there were four different cadmium particle variants depending upon which of the four $\{111\}_{Al}$ planes was parallel to the $\{0001\}_{Cd}$ plane. Fig. 3a shows a typical selected area electron diffraction pattern with superimposed $[111]_{Al}$, $[0001]_{Cd}$, $[03\bar{3}1]_{Cd}$, $[3\bar{3}01]_{Cd}$ and $[30\bar{3}1]_{Cd}$ zones from the aluminium matrix and four cadmium particle variants respectively. This orientation shows the {220} diffraction spots from the $[111]_{Al}$ zone, and the $\{10\bar{1}0\}$ diffraction spots from the $[0001]_{Cd}$ zone, but diffraction spots from the other three cadmium particle variants were obscured by the $\{220\}_{Al}$ diffraction spots, as can be seen on the schematic diffraction pattern in Fig. 3b. Fig. 3c shows a bright field image corresponding to the diffraction pattern in Fig. 3a, and Fig. 3d shows a dark field image from the same region taken with the $(10\bar{1}0)_{Cd}$ diffraction spot from the $[0001]_{Cd}$ zone. As expected from the schematic diffraction pattern in Fig. 3b, only a quarter of the cadmium particles in the bright field image in Fig. 3c were illuminated in the $(10\bar{1}0)_{Cd}$ dark field image in Fig. 3d, since the $\{10\bar{1}0\}_{Cd}$ diffraction spots were generated by only one of the four cadmium particle variants.

The as-melt spun cadmium particle shape was found to be distorted cuboctahedral, bounded by six curved $\{100\}_{Al}//\{20\bar{2}3\}_{Cd}$ facets, six curved $\{111\}_{Al}//\{40\bar{4}3\}_{Cd}$ facets, and the two flat $\{111\}_{Al}//\{0001\}_{Cd}$ facets, as schematically shown in Fig. 4a. Typical as-melt spun cadmium particle cross-sectional shapes with the electron beam parallel to the $[\bar{1}10]_{Al}$ zone are shown in Fig. 4b, with corresponding selected area and schematic diffraction patterns in Fig. 4c and d. Three types of cadmium particle cross-sectional shape can be seen in Fig. 4b. The particle marked 1 in Fig. 4b belonged to variant 1, with a distorted hexagonal shape bounded by pairs of $(111)_{Al}//(0001)_{Cd}$, $(11\bar{1})_{Al}//(\bar{4}403)_{Cd}$ and $(001)_{Al}//(\bar{2}203)_{Cd}$ facets; the particle marked 2 in Fig. 4b belonged to variant 2, with a distorted hexagonal shape bounded by pairs of $(11\bar{1})_{Al}//(0001)_{Cd}$, $(111)_{Al}//(\bar{4}403)_{Cd}$ and $(001)_{Al}//(2\bar{2}03)_{Cd}$ facets; the particle marked 3 in Fig. 4b belonged to variant 3 or 4, with a distorted hexagonal shape bounded by pairs of $(111)_{Al}//(0\bar{4}43)_{Cd}$, $(11\bar{1})_{Al}//(40\bar{4}3)_{Cd}$ and $(001)_{Al}//(20\bar{2}3)_{Cd}$ facets.

After heat treatment for 300 sec at 350 °C, above the cadmium melting point, there was no change in either the cadmium particle shape, or the orientation relationship between the cadmium particles and the aluminium matrix. After heat treatment, however, for 10^5 sec at 300 °C, below the cadmium melting point, the cadmium particles became elongated to increase the surface area and decrease the separation of the two $\{111\}_{Al}//\{0001\}_{Cd}$ facets, as shown schematically in Fig. 5a. Typical annealed cadmium particle cross-sectional shapes with the electron beam parallel to the $[\bar{1}10]_{Al}$ zone are shown in Fig. 5b, with corresponding selected area and schematic diffraction patterns in Fig. 5c and d. Again, three types of cadmium particle shape can be seen in Fig. 5b. The particle marked 1 in Fig. 5b belonged to variant 1, with a distorted hexagonal shape bounded by pairs of $(111)_{Al}//(0001)_{Cd}$, $(11\bar{1})_{Al}//(\bar{4}403)_{Cd}$ and $(001)_{Al}//(\bar{2}203)_{Cd}$ facets; the particle marked 2 in Fig. 5b belonged to variant 2, with a distorted hexagonal shape bounded by pairs of $(11\bar{1})_{Al}//(0001)_{Cd}$, $(111)_{Al}//(\bar{4}403)_{Cd}$ and $(001)_{Al}//(2\bar{2}03)_{Cd}$ facets; the particle marked 3 in Fig. 5b belonged to variant 3 or 4, with a distorted hexagonal shape bounded by pairs of $(111)_{Al}//(0\bar{4}43)_{Cd}$, $(111)_{Al}//(40\bar{4}3)_{Cd}$ and $(001)_{Al}//(20\bar{2}3)_{Cd}$ facets.

3.2. Surface energy anisotropy

The shapes of individual cadmium particles were monitored as a function of temperature during *in situ* step heating in the transmission electron microscope, using specimens of the melt-spun Al–4.5wt%Cd alloy equilibrated by annealing for 10^5 sec at 300 °C. Before heating in the electron microscope, specimens were tilted until the electron beam was parallel to an aluminium $\langle 110\rangle$ zone. As shown in Figs 4 and 5, with this specimen orientation all the cadmium particle facets were parallel to the electron beam, so that the observed separation of each pair of opposite facets was equal to the true separation, and from the Gibbs–Wulff theorem was directly proportional to the facet surface energy [41, 42]. After careful orientation in this way, specimens were heated in steps of 20 to 50 K up to a maximum temperature of 420 °C, with

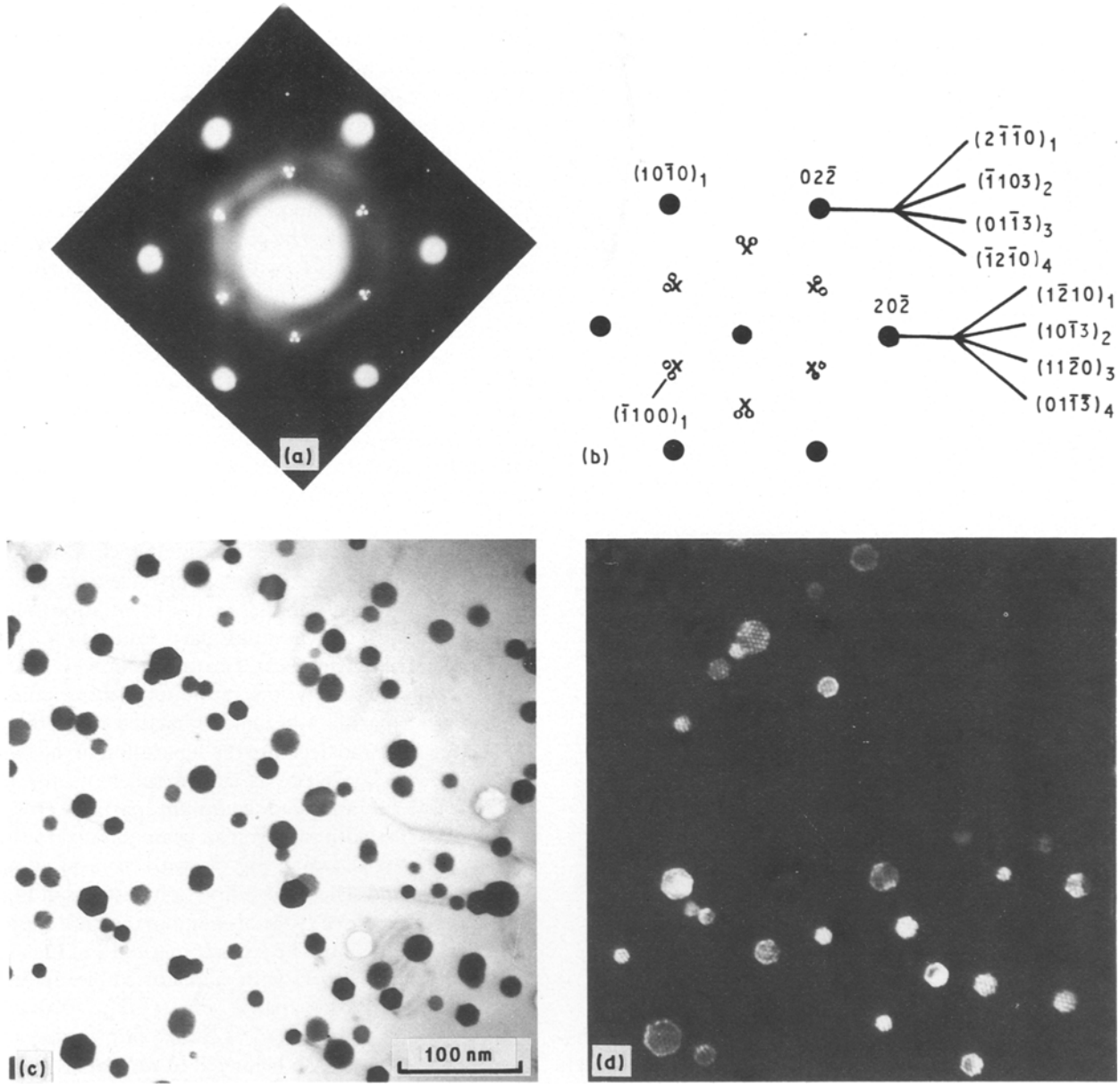

Figure 3 (a) Selected area diffraction pattern from as-melt spun Al–4.5wt%Cd, showing superimposed $[111]_{Al}$, $[0001]_{Cd}$, $[03\bar{3}1]_{Cd}$, $[3\bar{3}01]_{Cd}$ and $[30\bar{3}1]_{Cd}$ zones from the aluminium matrix and cadmium particle variants 1 to 4 respectively; (b) schematic diffraction pattern corresponding to (a) with crosses corresponding to diffraction spots from the $[0001]_{Cd}$ zone, filled circles corresponding to superimposed diffraction spots from the $[111]_{Al}$ zone and all four cadmium particle variants, and open circles corresponding to double diffraction; (c) bright field micrograph corresponding to (a); (d) dark field micrograph from the same area as (c) and formed with the $(10\bar{1}0)_{Cd}$ spot.

the cadmium particle shape recorded at each temperature after an equilibrating anneal of either 600 sec below or 180 sec above the cadmium melting point of 321 °C. Approximate diffusion calculations indicated that these times were sufficient for equilibration of the 5 to 120 nm cadmium particles at all temperatures above about 200 °C. This was confirmed by *in situ* step cooling experiments, in which the cadmium particles changed shape in a reverse sequence to that seen during heating. During step cooling, the different cadmium particle shape variants all re-appeared after solidification, with no time lag from insufficient equilibration during annealing.

Fig. 6 shows a selected area diffraction pattern and two typical series of bright field images of the cadmium particle shapes as a function of temperature during *in situ* heating in the transmission electron microscope. The cadmium particle shape in series 1 corresponded to variant 3 or 4, i.e. was similar to the cadmium particle marked 3 in Fig. 5b; and the cadmium particle shape in series 2 corresponded to variant 1, i.e. was similar to the cadmium particle marked 1 in Fig. 5b. Almost identical results were obtained for a number of different cadmium particles during heating, and Fig. 7 shows the resulting variation of average surface energy anisotropy as a function of temperature. The cadmium particle shape was constant between room temperature and the cadmium melting point of 321 °C, with the $\{100\}_{Al}//\{20\bar{2}3\}_{Cd}$ surface energy on average 40% greater than the $\{111\}_{Al}//\{0001\}_{Cd}$ surface energy, and 10% greater than the $\{111\}_{Al}//\{40\bar{4}3\}_{Cd}$ surface energy. When the cadmium particles melted, the $\{100\}_{Al}//\{20\bar{2}3\}_{Cd}$ facet disappeared, and the $\{111\}_{Al}//\{40\bar{4}3\}_{Cd}$ and $\{111\}_{Al}//\{0001\}_{Cd}$ surface energies became equal. However, the $\{111\}_{Al}$ facets did not disappear when

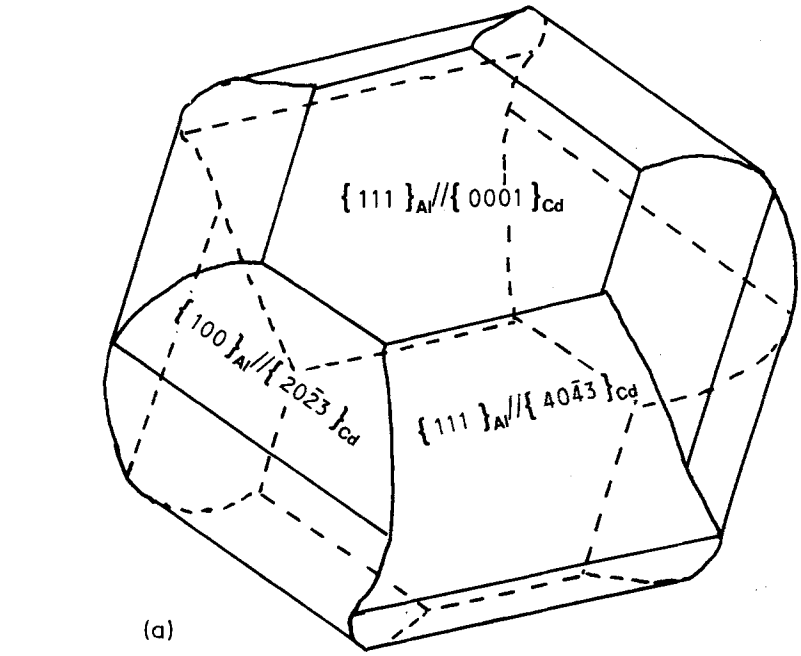

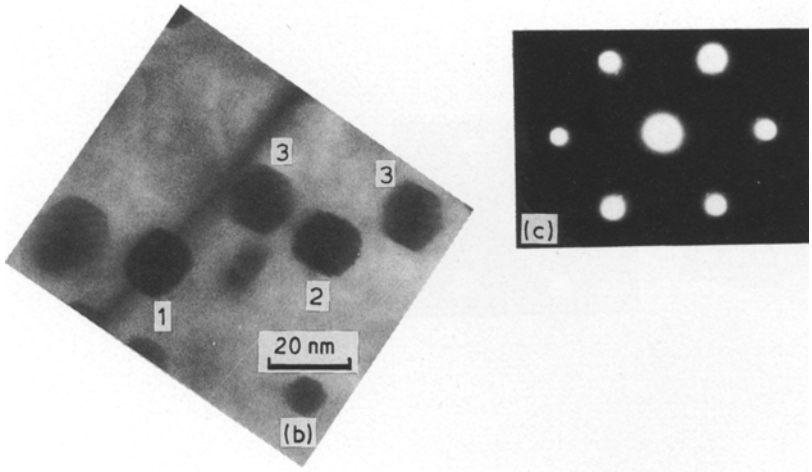

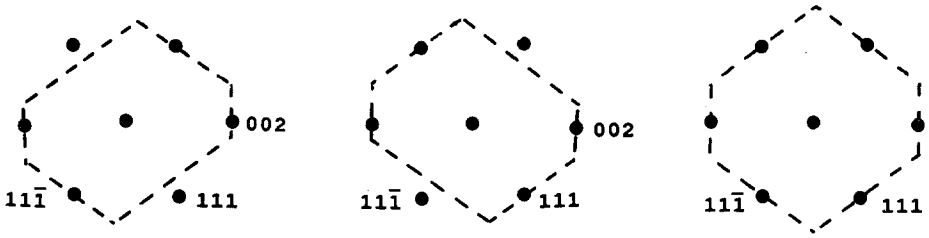

(d)

Figure 4 (a) Schematic diagram of as-melt spun cadmium particle distorted cuboctahedral shape; (b) bright field micrograph from as-melt spun Al–4.5wt%Cd showing the distorted hexagonal cross-sections of cadmium particles perpendicular to the $[\bar{1}10]_{Al}$ zone axis; (c) selected area diffraction pattern corresponding to (b) showing $[\bar{1}10]$ zone of aluminium matrix; (d) schematic diffraction pattern cadmium particle cross-sections.

the cadmium particles melted, and the surface energy anisotropy decreased gradually from 1.1 to 1.0, as the temperature increased above the cadmium melting point from 321 to about 450 °C.

3.3. Cadmium particle solidification

Fig. 8a to c show typical cadmium solidification exotherms from melt-spun Al–4.5wt%Cd obtained at cooling rates of 2, 5 and 10 K min^{-1} respectively in the differential scanning calorimeter. The cadmium particles always solidified with a single sharp exotherm at an onset temperature close to 265 °C, but the shape of the cadmium particle solidification exotherms depended upon the imposed cooling rate in the calorimeter. Table I gives full details of the measured onset, peak and end temperatures and peak heights of the cadmium particle solidification exotherms, obtained from a series of differential scanning calorimeter experiments similar to those shown in Fig. 8a to c. At each cooling rate, the onset, peak and end temperatures of the cadmium particle solidification exotherms were reproducible to within ± 0.2 to 0.3 K from specimen to specimen, as can be seen in Fig. 8a to

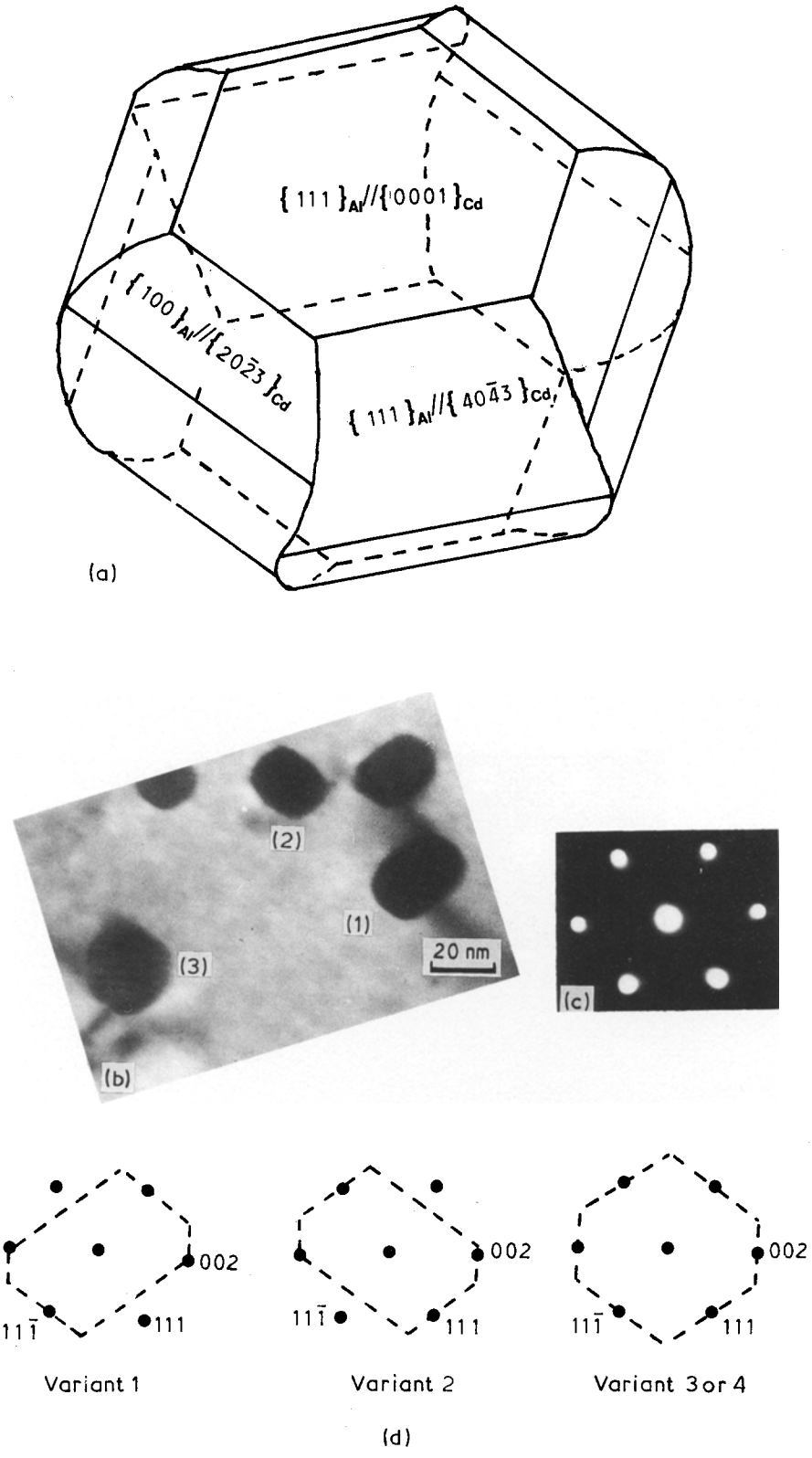

Figure 5 (a) Schematic diagram of equilibrium cadmium particle distorted cuboctahedral shape; (b) bright field micrograph from melt-spun Al–4.5wt%Cd after heat treatment for 10^5 sec at 300 °C, showing the distorted hexagonal cross-sections of Cd particles perpendicular to the $[\bar{1}10]_{Al}$ zone axis; (c) selected area diffraction pattern corresponding to (b) showing $[\bar{1}10]$ zone of aluminium matrix; (d) schematic diffraction pattern and cadmium particle cross-sections.

c and Table I. Fig. 9a and b show the variation of solidification onset, peak and end temperatures and exothermic peak height as functions of cooling rate in the calorimeter. The solidification onset temperature was independent of cooling rate, but the peak and end temperatures decreased and the peak height increased with increasing cooling rate.

4. Discussion

4.1. Alloy microstructure

The rapidly solidified microstructure of melt-spun hypomonotectic Al–4.5wt%Cd is shown in Fig. 1 and corresponds to a solidification sequence which can be described as follows.

(1) *Monotectic solidification.* For a composition of 4.5wt%Cd, the gap between the liquidus and monotectic temperatures is less than 5 K [43]. During rapid solidification, primary aluminium dendritic solidification is either suppressed completely or limited to an insignificant extent. On cooling below the monotectic temperature of 650 °C [43], the Al–4.5wt%Cd liquid solidifies at high speed by a duplex monotectic reaction, producing small Cd–1.3wt%Al liquid droplets with sizes of 5 to 120 nm embedded in a matrix of solid aluminium. The irregular cadmium particle mono-

tectic microstructure in Fig. 1 is consistent [44, 45] with a relative low value of ~ 100 Ksec mm^{-2} for the ratio of thermal gradient to solidification velocity G/V during melt-spinning, estimated from

$$G/V = (T_m - T_r)t/y^2 \quad (1)$$

where T_m is the melt temperature, T_r the room temperature, y the section size and t the solidification time.

(2) *Droplet coarsening.* During cooling from the monotectic temperature of 650 °C to the eutectic temperature of 320 °C [43], the average diffusion distance X of cadmium in solid aluminium is approximately 10 nm, estimated from

$$X^2 = 4Dt \quad (2)$$

where D is the average cadmium diffusivity in solid aluminium and t is the cooling time [46]. The diffusion distance is relatively small compared with the cadmium interparticle spacing of 140 nm, and there is insufficient time for significant cadmium particle coarsening to take place. During cooling from 650 to 320 °C, the solubility of aluminium in the cadmium droplets decreases from 1.3wt% to zero by deposition on the surrounding aluminium matrix.

(3) *Droplet solidification.* On cooling below the eutectic temperature of 320 °C [43], the cadmium droplets solidify by heterogeneous nucleation on the $\{111\}$ facets of the surrounding aluminium matrix as shown in Fig. 6, with an epitaxial orientation relationship of $\{111\}_{Al}//\{0001\}_{Cd}$ and $\langle 110\rangle_{Al}//\langle 11\bar{2}0\rangle_{Cd}$ as shown in Fig. 3. In each aluminium grain, four cadmium particle variants are formed depending upon which of the four $\{111\}_{Al}$ planes is parallel to $\{0001\}_{Cd}$. Transmission electron micrographs and electron diffraction patterns such as Fig. 4a to d show that the resulting solid cadmium particles embedded in the aluminium matrix have a distorted cuboctahedral shape, bounded by six curved $\{100\}_{Al}//\{20\bar{2}3\}_{Cd}$ facets, six curved $\{111\}_{Al}//\{40\bar{4}3\}_{Cd}$ facets and two flat $\{111\}_{Al}//\{0001\}_{Cd}$ facets. Details of the cadmium particle solidification behaviour are clarified by the differential scanning calorimeter results obtained during subsequent heat treatment, and are discussed further in Sections 4.3 to 4.5.

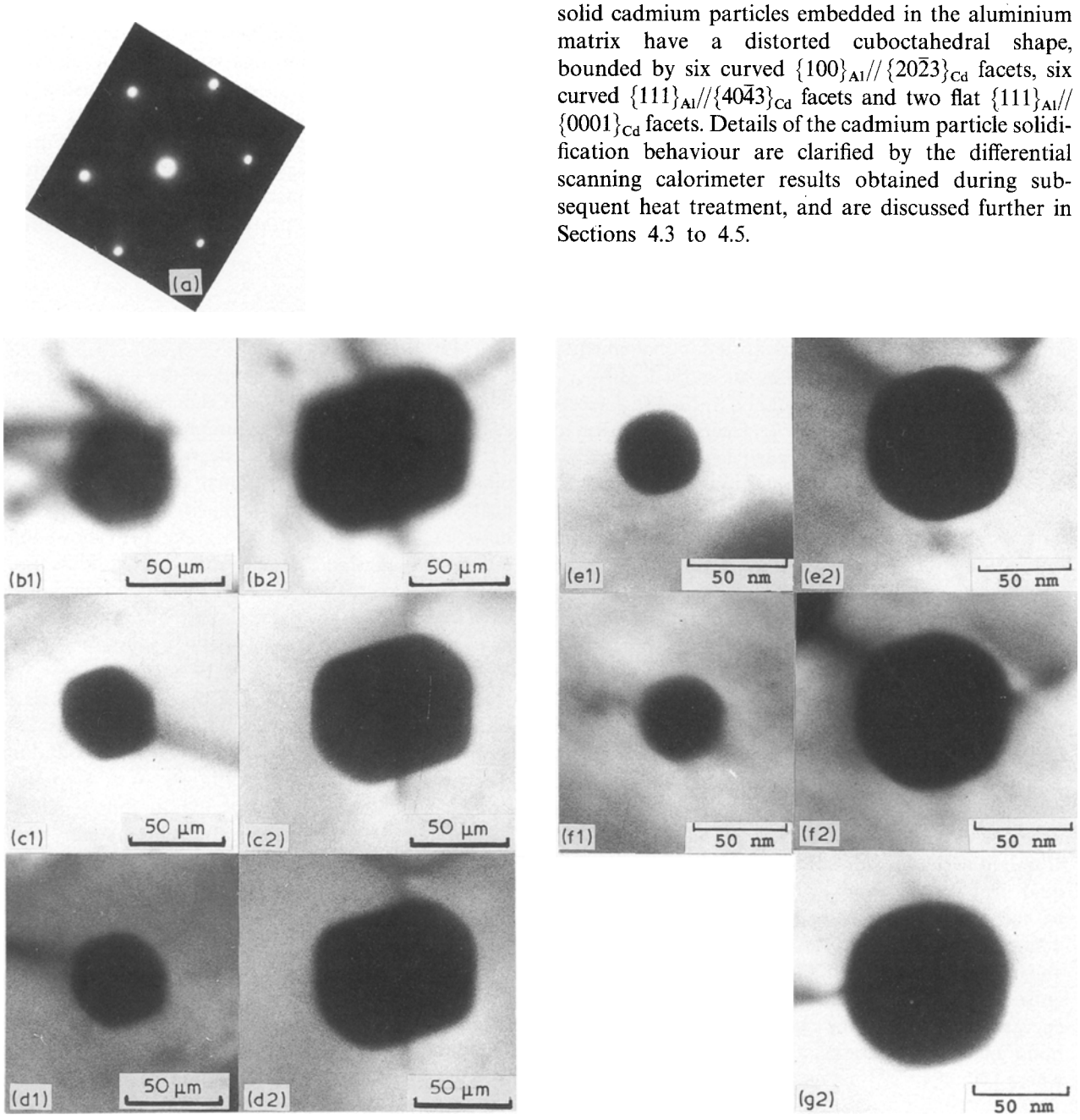

Figure 6 Sequence of transmission electron micrographs showing the variation in shape of two cadmium particles in melt-spun Al–4.5wt%Cd after heat treatment for 10^5 sec at 300 °C, as a function of temperature during subsequent *in situ* heating: (a) selected area diffraction pattern showing $[\bar{1}10]$ zone of aluminium matrix; (b1) and (b2) room temperature; (c1) and (c2) 220 °C; (d1) and (d2) 270 °C; (e1) and (e2) 320 °C; (f1) and (f2); 350 °C; (g2) 370 °C.

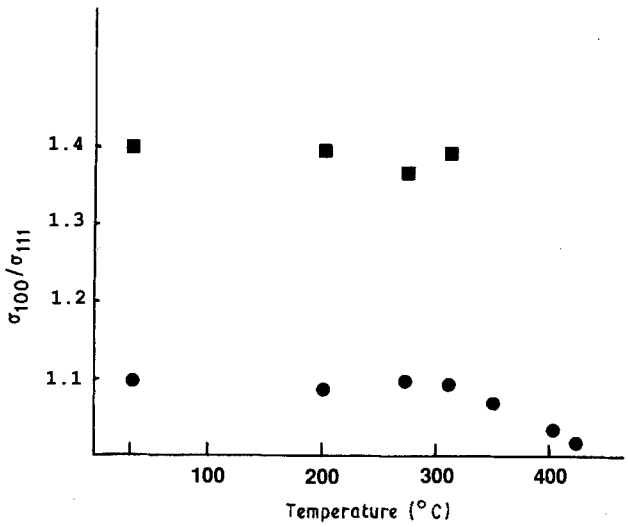

Figure 7 Aluminium–cadmium surface energy anisotropy as a function of temperature from measurements of facet separation in melt-spun Al–4.5wt%Cd after heat treatment for 10^5 sec at 300 °C during subsequent *in situ* heating in the transmission electron microscope. Filled squares correspond to $\{111\}_{Al}//\{0001\}_{Cd}$ facets, and filled circles correspond to $\{111\}_{Al}//\{40\bar{4}3\}_{Cd}$ facets.

4.2. Surface energy anisotropy

Transmission electron micrographs and electron diffraction patterns such as Figs 3 and 4 show that as-melt spun cadmium particles embedded in an aluminium matrix have a distorted cuboctahedral equilibrium shape, bounded by six curved $\{100\}_{Al}//\{20\bar{2}3\}_{Cd}$ facets, six curved $\{111\}_{Al}//\{40\bar{4}3\}_{Cd}$ facets and two flat $\{111\}_{Al}//\{0001\}_{Cd}$ facets. As shown in Figs 4 and 5, the cadmium particles become further elongated after annealing in the solid state for 10^5 sec at 300 °C, indicating that the as-melt spun cadmium particle shape is metastable. Measurements of facet separations during *in situ* heating in the transmission electron microscope are shown in Figs 6 and 7, and indicate that the small cadmium particles in annealed Al–4.5wt%Cd can equilibrate quickly during either heating and melting or cooling and solidification, even when the temperature changes rapidly. Liquid cadmium particle shapes embedded in an aluminium matrix above the cadmium melting point are very similar to the liquid lead particle shapes embedded in an aluminium matrix above the lead melting point which were seen by Moore *et al.* [47]. Thus, solid aluminium–liquid cadmium and solid aluminium– liquid lead surface energy anisotropies are controlled by the crystallography and atomic structure of the different aluminium surfaces at temperatures just above the cadmium and lead melting points. The anisotropy of solid aluminium–solid cadmium surface energy anisotropy can be explained by near neighbour bond energy calculations, as discussed in detail elsewhere [47, 48].

4.3. Cadmium particle solidification

Differential scanning calorimeter traces such as in Fig. 8a to c give detailed information about the cadmium particle solidification kinetics in melt-spun hypomonotectic Al–4.5wt%Cd. The large number of cadmium particles ensures reproducibility in the differential scanning calorimeter traces. The small size of the cadmium particles ensures that their solidification kinetics are dominated by nucleation, since each particle must be nucleated independently during cooling below the melting point in the differential scanning calorimeter. The cadmium particle solidification behaviour in melt-spun hypomonotectic Al–4.5wt%Cd can be described as follows. On cooling below the melting point, cadmium particles containing catalytic trace impurities nucleate and solidify with a variable undercooling because of the variable catalytic potency of the trace impurities. Because of the large number and small size of the cadmium particles, too few are nucleated by catalytic trace impurities to be detected in the differential scanning calorimeter. Below 265 °C, all the cadmium particles which have not been nucleated by catalytic trace impurities are nucleated by the surrounding aluminium matrix, with an epitaxial aluminium–cadmium orientation relationship as shown in Fig. 3, and a sharp exothermic peak in the differential scanning calorimeter as shown in Fig. 8a to c. As shown in Figs 6 and 7, cadmium particle nucleation can take place on the {111} aluminium facets which survive above the cadmium melting point.

4.4. Nucleation kinetics

The equilibrium melting point of the cadmium particles in melt-spun Al–4.5wt%Cd may not be the same as the bulk equilibrium cadmium melting point of 321 °C, because of pressure effects caused by a combination of differential thermal contraction, solidification shrinkage and capillarity. Previous work, however, on melt-spun Al–4.5wt%Cd [49] shows that differential thermal contraction and solidification shrinkage stresses are relieved by a combination of cavitation and vacancy creep, and that capillary forces have an insignificant effect on the cadmium particle melting point.

In melt-spun Al–4.5wt%Cd, the 5 to 120 nm sized cadmium particles begin to nucleate and solidify at a temperature of $\sim$ 265 °C, $\sim$ 56 K below the cadmium melting point as shown in Fig. 8a to c. Complete particle solidification is expected to follow almost instantaneously after nucleation for such small cadmium particles at relatively high undercooling. At any temperature T below the cadmium particle melting point, the fraction of solid particles Z is therefore given by the differential equation [49]:

$$dZ/dt = I(1 - Z) \quad (3)$$

where I is the nucleation frequency within each cadmium particle. With decreasing temperature below the cadmium particle melting point, the cadmium particle solidification rate dZ/dt increases with increasing nucleation frequency I, reaches a maximum, and then decreases as the fraction of solid particles Z approaches 1. At a constant cooling rate $\dot{T}$, the cadmium particle solidification rate has its maximum value

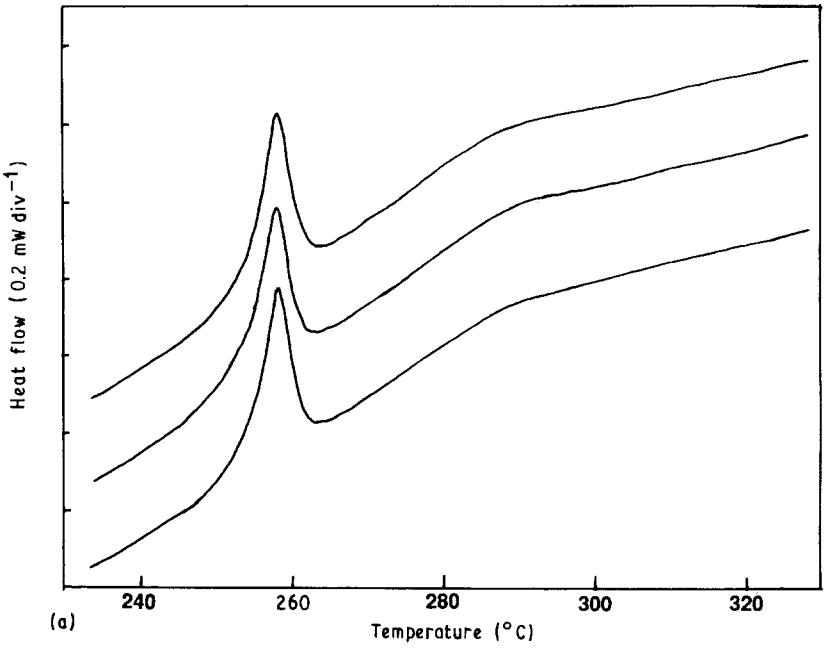

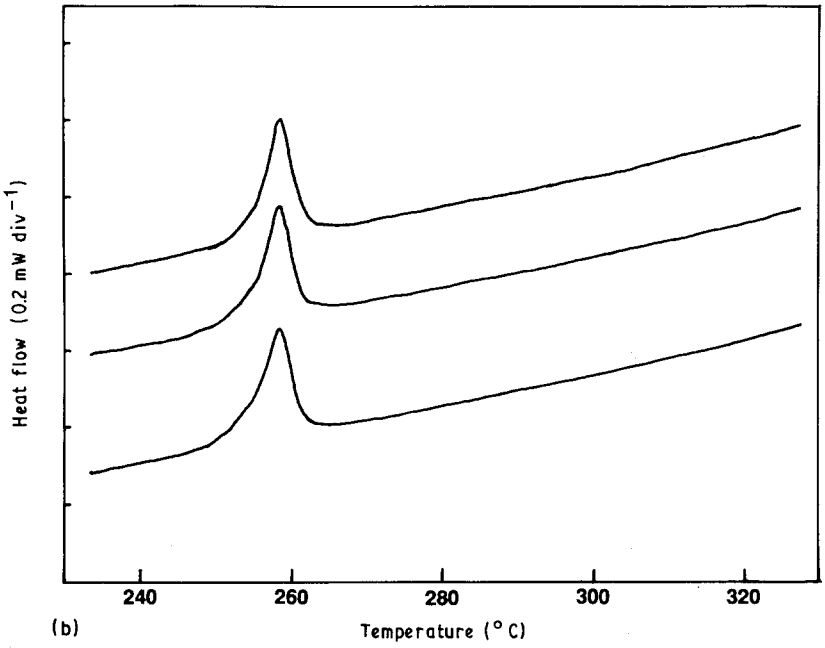

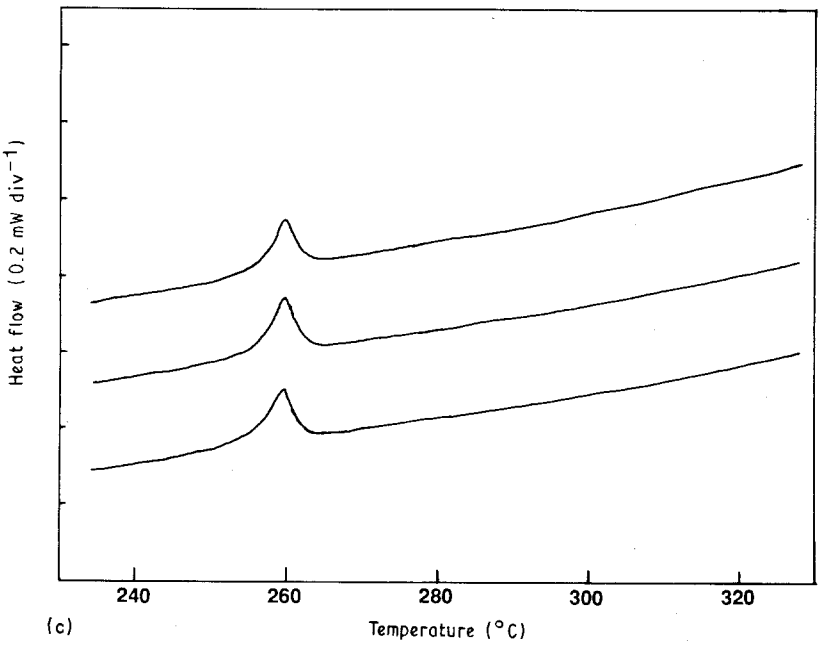

Figure 8 Differential scanning calorimeter traces of cadmium particle solidification exotherms from melt-spun Al–4.5wt%Cd as a function of cooling rate: (a) 10 K min^{-1}; (b) 5 K min^{-1}; and (c) 2 K min^{-1}.

TABLE I Onset, peak and end temperatures and peak heights of cadmium particle solidification exotherms during cooling melt-spun hypomonotectic Al–4.5wt%Cd in the differential scanning calorimeter.

Cooling rate ($K\,min^{-1}$)	Number of specimens	Onset temperature (°C)	Peak temperature (°C)	End temperature (°C)	Peak height ($mW\,g^{-1}$)
10.0	8	264.7 ± 0.2	258.0 ± 0.2	248.1 ± 0.3	44.3 ± 2.5
5.0	8	265.0 ± 0.3	258.6 ± 0.2	249.7 ± 0.3	31.5 ± 2.5
2.0	8	265.1 ± 0.3	259.5 ± 0.2	252.6 ± 0.3	14.2 ± 1.0
1.0	5	264.8 ± 0.2	260.2 ± 0.1	254.5 ± 0.3	7.5 ± 0.5
0.5	2	265.4 ± 0.1	260.6 ± 0.1	256.0 ± 0.3	4.4 ± 0.2

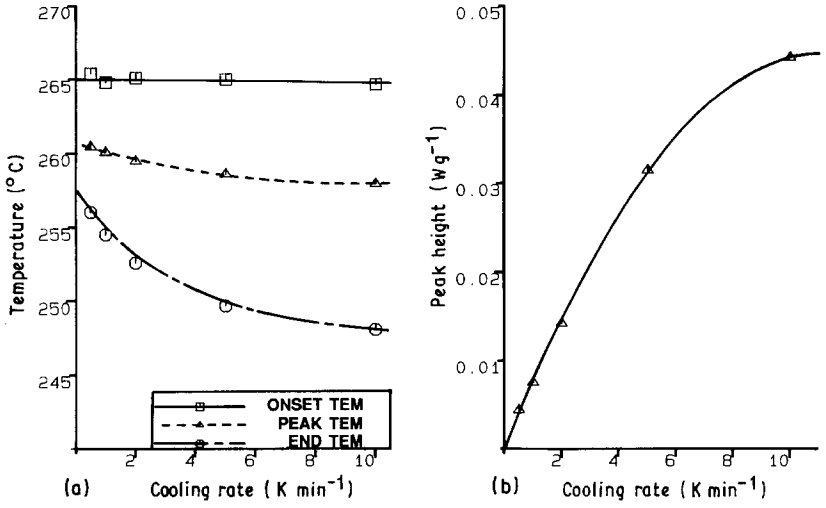

Figure 9 Exothermic peak shape from cadmium particle solidification in melt-spun Al–4.5wt%Cd as a function of cooling rate in the differential scanning calorimeter:(a) solidification onset (□), peak (△) and end (○) temperatures; and (b) exothermic peak height.

when $(d/dT)(dZ/dt) = -\dot{T}^{-1}\,d^2Z/dt^2 = 0$, which by differentiating Equation 3 is equivalent to

$$dI/dt = -\dot{T}\,dI/dT = I^2 \quad (4)$$

Fig. 10 shows schematically the heterogeneous nucleation of a hemispherical cap of solid cadmium on a catalytic $\{hkl\}$ facet of the aluminium matrix surrounding a liquid cadmium particle in melt-spun Al–4.5wt%Cd. The nucleation frequency I within each cadmium particle is given by [50, 51]

$$I = A\exp[-B/(T_m - T)^2T] \quad (5)$$

where T_m is the cadmium particle melting point, $A = N_c(kT/h)\exp(-Q/kT)$, N_c the number of catalytic nucleation sites per cadmium particle, k and h Boltzmann's and Plank's constants, respectively, Q the activation free energy for transporting a cadmium atom across the cadmium solid–liquid interface, $B = K\sigma^3T_m^2f(\theta)/kL^2$, K a shape factor, equal to $16\pi/3$ for a hemispherical cap shaped nucleus, σ the cadmium solid–liquid surface energy, $f(\theta) = (2 - 3\cos\theta + \cos^3\theta)/4$, θ the contact angle at the solid aluminium–solid cadmium–liquid cadmium triple point as shown in Fig. 10, and L the cadmium latent heat of solidification per unit volume.

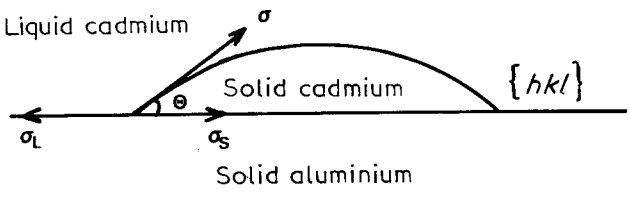

Figure 10 Schematic diagram of the heterogeneous nucleation of cadmium particle solidification on a catalytic $\{hkl\}$ facet of the surrounding aluminium matrix during heating and cooling of melt-spun Al–4.5wt%Cd in the differential scanning calorimeter.

4.5. Contact angle

On differential scanning calorimeter traces such as shown in Fig. 8a to c, the cadmium particle solidification rate dZ/dt at each temperature is directly proportional to the measured excess heat flow, i.e. to the height of the exothermic solidification peak. The fraction of solid cadmium particles Z can also be obtained at each temperature by partial integration of the exothermic solidification peak. Equations 3 to 5 and the differential scanning calorimeter traces in Fig. 8a to c can then be used in several different ways to calculate the contact angle θ at the solid aluminium–solid cadmium–liquid cadmium triple point, and the number of catalytic nucleation sites per cadmium particle N_c [49].

(1) From Equations 3 and 5, the cadmium particle solidification onset temperature is independent of cooling rate in the differential scanning calorimeter, in agreement with the experimental measurements shown in Fig. 9 for melt-spun Al–4.5wt%Cd. From Equations 3 and 5, the cadmium particle solidification onset temperature is given by $(dZ/dt)_{onset} = (dZ/dt)_{z=0} = I = (dZ/dt)^*$, where $(dZ/dt)^*$ is the detection limit of the calorimeter. The calorimeter traces in Fig. 8a to c were obtained with a typical specimen size of 18 mg and a calorimeter sensitivity of 0.1 mW, corresponding to a detection limit of $2.2 \times 10^{-3}\,sec^{-1}$. Assuming that all the aluminium atoms at

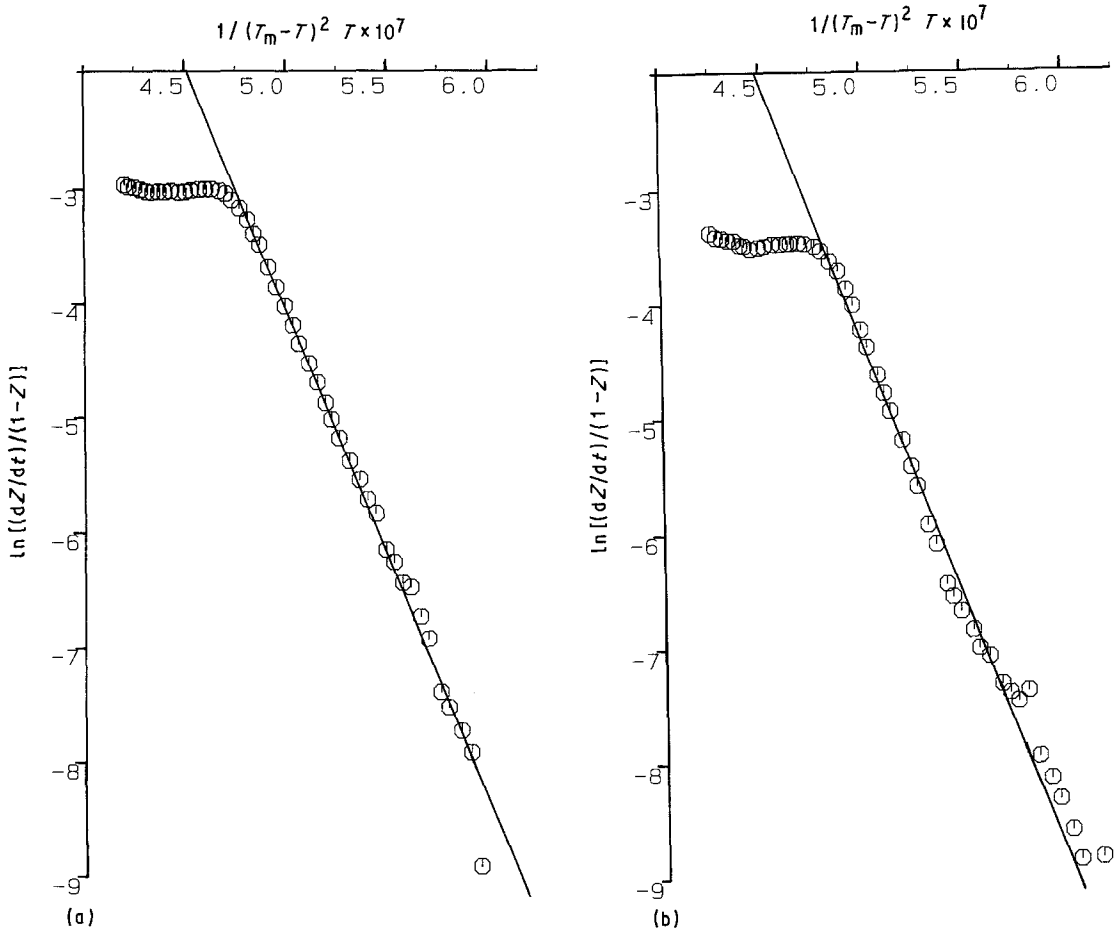

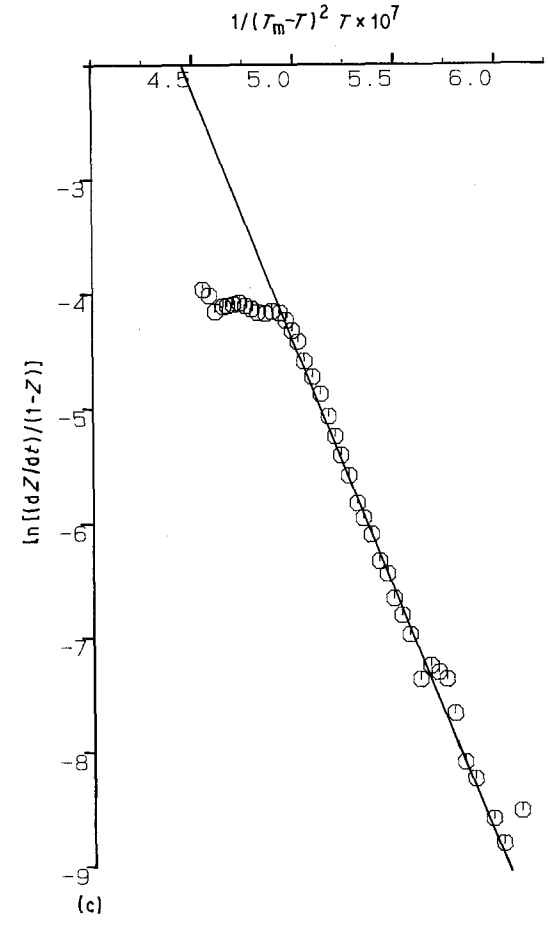

Figure 11 Differential scanning calorimeter traces of cadmium particle solidification exotherms from melt-spun Al–4.5wt%Cd, replotted from Fig. 8 according to Equation 3 and 5 in the form $\ln[(dZ/dt)/(1-Z)]$ against $1/(T_m - T)^2T$: (a) 10 K min^{-1}; (b) 5 K min^{-1}; and (c) 2 K min^{-1}.

the surface of the $\{111\}_{Al}$ facets of the cadmium particles can act as catalytic nucleation sites, $N_c = 1.4 \times 10^4$ for an average cadmium particle diameter of 20 nm. Taking $\exp(-Q/kT) = 10^{-2}$ [52, 53], $\sigma = 87$ mJ m^{-2} [52] and $L = 441$ mJ m^{-3} [53], a solidification onset temperature of 265 °C gives $f(\theta) = 0.048$ and $\theta = 43°$.

(2) Equations 3 and 5 can also be used to describe the shape of individual cadmium particle solidification exotherms in the differential scanning calorimeter. Combining Equations 3 and 5, $\ln[(dZ/dt)/(1-Z)]$ varies linearly with $1/(T_m - T)^2T$, with a slope and intercept of $-B$ and $\ln A$ respectively. Fig. 11a to c show cadmium particle solidification exotherms from melt-spun Al–4.5wt%Cd, obtained at cooling rates of 10, 5 and 2 K min^{-1} respectively in the differential scanning calorimeter, and replotted in the form $\ln[(dZ/dt)/(1-Z)]$ against $1/(T_m - T)^2T$. The linear variation predicted by Equations 3 and 5 is obeyed well over the temperature range between the solidification onset and peak temperatures. Best fit slopes and intercepts give values of A and B which correspond to contact angles θ in the range 38° to 40°, and numbers of catalytic nucleation sites per cadmium particle N_c in the range 7.5×10^{-4} to 0.1.

(3) From Equations 3 and 5, the maximum cadmium particle solidification rate $(dZ/dt)_{max}$ is given by [49]

$$(dZ/dt)_{max} = A(1 - Z_{max}) \exp[-B/(T_m - T_{max})^2 T_{max}] \quad (6)$$

and corresponds to a temperature T_{max}, which can be obtained from Equation 4 after differentiating Equation 5 with A approximately independent of temperature [50, 51]

$$B\dot{T}(3T_{max} - T_m)/A(T_m - T_{max})^3 T_{max}^2 = \exp[-B/(T_m - T_{max})^2 T_{max}] \quad (7)$$

Equations 6 and 7 describe the variation in shape of cadmium particle solidification exotherms as a function of cooling rate in the differential scanning calorimeter, as shown in Figs 8 and 9. From Equations 6 and 7, the cadmium particle solidification peak temperature T_{max} decreases and the exothermic peak height $(dZ/dt)_{max}$ increases with increasing cooling rate, in agreement with the experimental results shown in Fig. 9 for melt-spun Al–4.5wt%Cd. From Equation 6, $\ln[(dZ/dt)_{max}/(1 - Z_{max})]$ varies linearly with $1/(T_m - T_{max})^2 T_{max}$, with a slope and intercept of $-B$ and $\ln A$ respectively; from Equation 7, $\ln [\dot{T}(3T_{max} - T_m)/(T_m - T_{max})^3 T_{max}^2]$ also varies linearly with $1/(T_m - T_{max})^2 T_{max}$, with a slope and intercept of $-B$ and $\ln (A/B)$ respectively. Fig. 12a and b show the cooling rate variation of cadmium particle solidification peak temperature and exothermic peak height respectively, replotted from Fig. 9 according to Equations 6 and 7. Best fit slopes and intercepts give values of A and B which correspond to contact angles θ of 43° and 41° and numbers of catalytic nucleation sites per cadmium particle N_c of 29.8 and 0.1 for the peak temperature and peak height variations, respectively.

The best method of analysing the cadmium particle solidification exotherms from differential scanning calorimeter traces such as shown in Fig. 8a to c is probably the cooling rate variation of peak shape shown in Fig. 12, which averages over a large number of independent differential scanning calorimeter experiments. The best measured value of contact angle θ at the solid aluminium–solid cadmium–liquid cadmium triple point is therefore 42°. The measured values of the number of catalytic nucleation sites per cadmium particle N_c are considerably smaller than the number of aluminium atoms on the $\{111\}_{Al}$ facets surrounding each cadmium particle, indicating that catalytic nucleation can only take place at special sites such as steps or dislocations on the $\{111\}_{Al}$ facets.

As shown in Fig. 10 the contact angle θ at the solid aluminium–solid cadmium–liquid cadmium triple point during cadmium particle solidification is determined by the relative magnitudes of the solid aluminium-liquid cadmium, solid aluminium–solid cadmium and solid cadmium–liquid cadmium surface energies, σ_L, σ_S and σ, respectively:

$$\cos\theta = (\sigma_L - \sigma_S)/\sigma \quad (8)$$

The surface energies σ_L and σ_S in Equation 8 depend upon the crystallography of the $\{hkl\}$ aluminium facet which catalyses the nucleation of solidification. Liquid cadmium particles can nucleate on the atomically ordered $\{111\}$ aluminium facets which survive above the cadmium melting point as shown in Figs 6 and 7, giving relatively small values of σ_S and θ, and a strong orientation relationship of $\{111\}_{Al}//\{0001\}_{Cd}$ and $\langle 110\rangle_{Al}//\langle 11\bar{2}0\rangle_{Cd}$ as shown in Fig. 3. Taking the best value of $\theta = 42°$, Equation 8 gives the difference in solid aluminium–liquid cadmium and solid aluminium–solid cadmium surface energies as $\sigma_L - \sigma_S = 65\ mJ\ m^{-2}$ on the $\{111\}$ aluminium facets.

5. Conclusions

The conclusions are as follows.

(1) The as-solidified microstructure of melt-spun hypomonotectic Al–4.5wt%Cd consists of a homogeneous distribution of faceted cadmium particles embedded in an aluminium matrix. The as-melt spun cadmium particle sizes range from 5 to 120 nm, with an average particle size of 20 nm. The cadmium particles are formed during monotectic solidification of the aluminium matrix, and have an irregular monotectic microstructure consistent with a relatively low value of $\sim 100\ K\ sec\ mm^{-2}$ of the ratio of thermal gradient to solidification velocity.

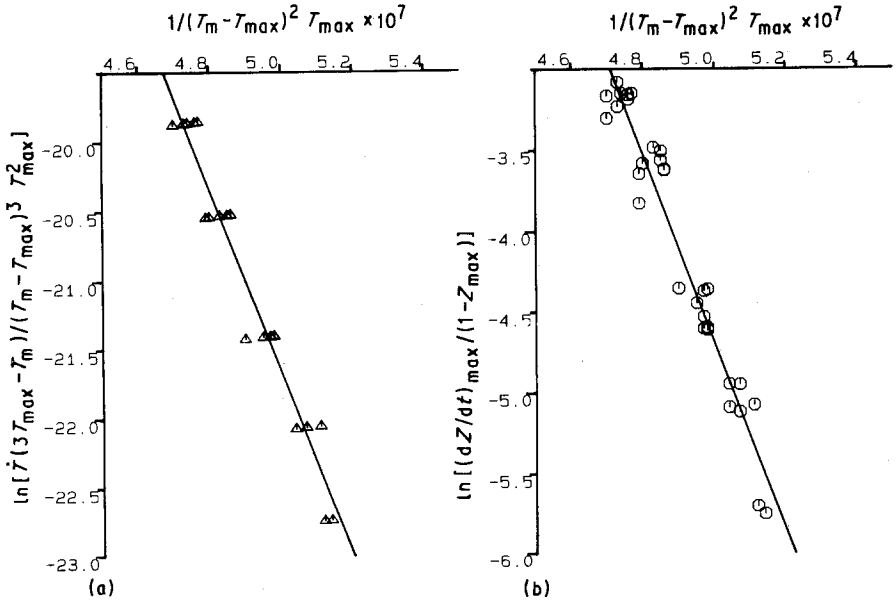

Figure 12 Cadmium particle solidification peak temperature and exothermic peak height for melt-spun Al–4.5wt%Cd as a function of cooling rate in the differential scanning calorimeter, replotted from Fig. 9 according to Equations 6 and 7 in the form: (a) $\ln [\dot{T}(3T_{max} - T_m)/(T_m - T_{max})^3 T_{max}^2]$ against $1/(T_m - T_{max})^2 T_{max}$; and (b) $\ln [(dZ/dt)_{max}/(1 - Z_{max})]$ against $1/(T_m - T_{max})^2 T_{max}$.

(2) The cadmium particles in melt-spun hypomonotectic Al–4.5wt%Cd exhibit an orientation relationship with the aluminium matrix of $\{111\}_{Al}//\{0001\}_{Cd}$ and $\langle 110\rangle_{Al}//\langle 11\bar{2}0\rangle_{Cd}$. In each aluminium grain, there are four cadmium particle variants depending upon which $\{111\}_{Al}$ plane is parallel to $\{0001\}_{Cd}$. The cadmium particles exhibit a distorted cuboctahedral shape, bounded by six curved $\{100\}_{Al}//\{20\bar{2}3\}_{Cd}$ facets, six curved $\{111\}_{Al}//\{40\bar{4}3\}_{Cd}$ facets, and two flat $\{111\}_{Al}//\{0001\}_{Cd}$ facets. The as-melt spun cadmium particles are metastable, and equilibrate during heat treatment just below the cadmium melting point, becoming elongated to increase the surface area and decrease the separation of the $\{111\}_{Al}//\{0001\}_{Cd}$ facets.

(3) The solid aluminium–solid cadmium surface energy anisotropy is constant over the temperature range between room temperature and the cadmium melting point of 321 °C, with the $\{100\}_{Al}//\{20\bar{2}3\}_{Cd}$ surface energy on average 40% greater than the $\{111\}_{Al}//\{0001\}_{Cd}$ surface energy and 10% greater the $\{111\}_{Al}//\{40\bar{4}3\}_{Cd}$ surface energy. The $\{100\}_{Al}//\{20\bar{2}3\}_{Cd}$ facets disappear, and the $\{111\}_{Al}//\{40\bar{4}3\}_{Cd}$ and $\{111\}_{Al}//\{0001\}_{Cd}$ surface energies become equal when the cadmium particles melt, and the surface energy anisotropy decreases gradually from 1.1 to 1 as the temperature increases above the cadmium melting point from 321 to about 450 °C.

(4) Solidification of cadmium particles embedded in an aluminium matrix is nucleated catalytically by the surrounding aluminium matrix on the $\{111\}_{Al}$ faceted surfaces with an undercooling of 56 K and a contact angle of 42°, in good agreement with the hemispherical cap model of heterogeneous nucleation.

Acknowledgements

We would like to thank Professor Sir Peter Hirsch for provision of laboratory facilities, Dr L. A. Johnson for help in manufacturing some of the melt-spun aluminium–cadmium materials, and Dr W. T. Kim for helpful discussions. One of us (DLZ) would like to thank the British Council and Chinese Committee of Education for the grant of a research studentship, and one of us (BC) would like to thank the General Electric Research Laboratory for the grant of an industrial fellowship.

References

1. J. W. CHRISTIAN, in "The Theory of Transformations in Metals and Alloys" (Pergamon, Oxford, 1975)
2. B. CANTOR, to be published
3. K. I. MOORE, D. L. ZHANG and B. CANTOR, *Acta Metall. Mater.* **38** (1990) 1327.
4. B. VONNEGUT, *J. Colloid Sci.* **3** (1948) 563
5. D. TURNBULL, *J. Chem. Phys.* **18** (1950) 768
6. J. H. PEREPEZKO, D. H. RASMUSSEN, I. E. ANDERSON and C. R. LOPER, "Solidification and Casting of Metals" (Metals Society, London, 1979) p. 169
7. J. H. PEREPEZKO, in "Rapid Solidification Processing: Principle and Technology", edited by R. Mehrabian, B. H. Kear and M. Cohen (Claitors, Boston, 1980) p. 56
8. Y. MIYAYAZAWA and G. POUND, *J. Cryst. Growth* **23** (1974) 45
9. J. H. PEREPEZKO and J. S. PAIK, *J. Non-Cryst. Solids* **61/62** (1984) 113
10. M. G. CHU, Y. SHIOHARA and M. C. FLEMINGS, *Met. Trans.* **15A** (1984) 1303
11. K. P. COOPER, I. E. ANDERSON and J. H. PEREPEZKO, in "Rapidly Quenched Metals IV", edited by K. Suzuki and T. Masumato (Japanese Institute of Metals, Tokyo, 1982) p. 107
12. B. A. MUELLER, J. J. RICHMOND, J. H. PEREPEZKO, in "Rapidly Quenched Metals V", edited by S. Steeb and H. Warlimont (North-Holland, Amsterdam, 1985) p. 47
13. J. H. PEREPEZKO, B. A. MUELLER, J. J. RICHMOND and K. P. COOPER, in "Rapidly Quenched Metals V", edited by S. Steeb and H. Warlimont (North-Holland, Amsterdam, 1985) p. 43
14. D. G. MacIASAAC, Y. SHIOHARA, M. G. CHU and M. C. FLEMINGS, in "Grain Refinement in Casting and Welds" (AIME, New York, 1983) p. 87
15. J. H. PEREPEZKO and J. S. SMITH, *J. Non-Cryst. Solids* **44** (1981) 65
16. D. TURNBULL and R. E. CECH, *J. Appl. Phys.* **21** (1950) 804
17. D. TURNBULL, *Trans. Met. Soc. AIME* **188** (1950) 1144
18. V. SCRIPOV in "Crystal Growth and Materials", edited by E. Kaldis and H. Scheel (North-Holland, Amsterdam, 1977) p. 327
19. M. J. STOWELL, *Phil. Mag.* **22** (1970) 1
20. F. J. BRADSHAW, M. E. GASPER and S. PEARSON, *J. Inst. Met.* **87** (1958–59) 15
21. B. E. SUNDQUIST and L. F. MONDOLFO, *Trans. Met. Soc. AIME* **221** (1961) 157
22. J. H. HOLLOMON and D. TURNBULL, *ibid.* **191** (1951) 803
23. R. E. CECH and D. TURNBULL, *ibid.* **206** (1956) 124
24. L. L. LACY, M. B. ROBINSON and J. J. RATHZ, *J. Cryst. Growth* **51** (1981) 47
25. A. J. DREHMAN and A. L. GREER, *Acta Metall.* **32** (1984) 323
26. A. J. DREHMAN and D. TURNBULL, *Scripta Metall.* **15** (1981) 543
27. C. S. KIMINAMI and P. K. SAHM, *Acta Metall.* **34** (1986) 2644
28. S. Y. SHIOHARA and P. G. WARD, *Can. Met. Quart* **3** (1964) 117
29. J. FEHLING and E. SCHEIL, *Z. Metallkde* **53** (1962) 593
30. J. WALKER, in "Physical Chemistry of Process Metallurgy", edited by G. R. St. Pierre (AIME, New York, 1961) p. 845
31. T. Z. KATTAMIS and M. C. FLEMINGS, *Trans. Met. Soc. AIME* **236** (1966) 1523
32. T. Z. KATTAMIS and M. C. FLEMINGS, *Met. Trans.* **1** (1970) 1449
33. T. Z. KATTAMIS, *J. Mater. Sci.* **5** (1970) 531
34. S. N. OJHA, P. RAMACHANDRARAO and T. R. ANANTHARAMAN, *Trans. Indian Inst. Met.* **36** (1983) 51
35. S. N. OJHA, T. R. ANANTHARAMAN and P. RAMACHANDRARAO, *J. Mater. Sci.* **17** (1982) 264
36. C. C. WANG and C. S. SMITH, *Trans Met. Soc. AIME* **188** (1950) 136
37. R. T. SOUTHIN and G. A. CHADWICK, *Acta Metall.* **26** (1978) 223
38. P. G. BOSWELL and G. A. CHADWICK, *ibid.* **28** (1980) 209
39. P. G. BOSWELL, G. A. CHADWICK, R. ELLIOT and F. R. SALE, in "Solidification and Casting of Metals" (Metals Society, London, 1979) p. 611
40. A. G. GILLEN and B. CANTOR, *Acta Metall.* **33** (1985) 1813
41. G. WULFF, *Z. Kristallog.* **53** (1901) 440
42. J. W. MARTIN and R. D. DOHERTY, in "Stability of Microstructure in Metallic Systems" (Cambridge University Press, Cambridge, 1976)
43. T. B. MASSALSKI, J. L. MURRAY, L. H. MENNETT and H. BAKERS, in "Binary Alloy Phase Diagrams" (American Society for Metals, Ohio, 1986)
44. B. DERBY, *Scripta Metall.* **8** (1984) 169
45. B. DERBY and J. J. FAVIER, *Acta Metall.* **31** (1983) 1123
46. P. G. SHEWMON, in "Diffusion in Solids" (McGraw-Hill Book Company, Wiley, 1963)

47. K. I. MOORE, K. CHATTOPADHYAY and B. CANTOR, *Proc. Roy. Soc.* **A414** (1987) 499
48. B. E. SUNDQUIST, *Acta Metall.* **12** (1964) 67
49. W. T. KIM, D. L. ZHANG and B. CANTOR, *Met. Trans.* in press
50. D. TURNBULL, *J. Appl. Phys.* **21** (1950) 1022
51. B. CANTOR and R. D. DOHERTY, *Acta Metall.* **27** (1979) 33
52. L. F. MONDOLFO, N. L. PARIST and G. J. KARDYS, *Mater. Sci. Eng.* **68** (1984–1985) 249
53. E. A. BRANDES and C. J. SMITHELLS, in "Metals Reference Handbook", 6th edn (Butterworths, London, 1983)

Received 3 October
and accepted 6 October 1989